

Ecosystem dynamics of zinc and manganese within a mine-waste impacted wetland

COLLEEN M. HANSEL¹, MATTHEW J. LA FORCE¹, STEPHEN SUTTON², AND SCOTT FENDORF^{*1}

¹Dept. of Geological and Environmental Sciences, Stanford University, Stanford, CA 94305, USA

²Consortium for Advanced Radiation Sources and Department of Geophysical Sciences,

University of Chicago, Chicago, IL 60637 USA

*fendorf@stanford.edu

Abstract—Wetland ecosystems, which serve as a natural filter for many environmental contaminants, influence the fate and transport of metals. The partitioning and specific binding mechanisms of metals within the soil, water, and plants have important implications for delineating potential bioavailability and/or release of metals upon changing physicochemical conditions within aquatic environments. Here we investigate the mechanisms of Mn and Zn partitioning and sequestration within a natural, mine-waste impacted wetland. The partitioning of Mn and Zn within the Cataldo wetland subsurface is dominantly in the mineral and plant root (*Typha latifolia*, *Phalaris arundinacea*, *Scirpus microcarpus*, *Equisetum arvense*) fractions while solution concentrations are negligible. Manganese and Zn concentrations of some plant species are equivalent to those of the soil and, in some cases, may exceed soil-associated Mn and Zn. Yet, owing to higher soil densities, the mass contributions are ≥ 10 -fold higher in the mineral fraction (Mn: 7,840 kg; Zn: 6,360 kg) relative to total plant roots (Mn: 707 kg; Zn: 319 kg). Manganese is predominantly present as a rhodochrosite-like (MnCO_3) phase within the soil and plant roots. Zinc, on the other hand, varies from a smithsonite-like (ZnCO_3) phase in the soil to its hydrated derivative, hydrozincite [$\text{Zn}_5(\text{OH})_6(\text{CO}_3)_2$], on the root surface. X-ray fluorescence microtomography and x-ray microprobe analysis reveal a strong correlation between Mn, Zn, and Ca on the surface of *P. arundinacea* roots. Manganese, Zn, and Ca exist as isolated nodules on the root surface with concentrations diminishing adjacent to these regions as well as in the interior of the root. Thus, carbonate ligands appear to be the dominant means by which Zn and Mn are sequestered within this ecosystem and may have a pronounced influence on metal sequestration in general.

1. INTRODUCTION

Several metal ions are essential for both plant and animal metabolism yet may have deleterious effects when exceeding threshold concentrations. The introduction of these toxic metals to terrestrial and aquatic environments is largely due to anthropogenic sources. Mining activities, for instance, have resulted in widespread contamination of surface waters, groundwater, soils, sediments, and vegetation. The Coeur d'Alene (CdA) mining district in the Idaho panhandle exemplifies the detrimental effects of mine-wastes on the environment. The CdA mining district is situated within the Lewis and Clark shear zone, composed of numerous faults trending primarily east-west and constituting an intracontinental plate boundary (Bennett et al., 1989). Mining of lode deposits allowed for the prosperity of more than 90 mines in the area and, hence, CdA earned the reputation as one of the most opulent mining districts worldwide. The district has the largest recorded Ag production in the world, as well as abundant quantities of Au, Cd, Cu, Pb, Sn, and Zn (Bennett et al., 1989). The primary economic minerals are galena (PbS), sphalerite (ZnS), and Ag-bearing tetrahedrite ($\text{Cu}_{12}\text{Sb}_4\text{S}_{13}$). The gangue minerals within the region are chiefly quartz (SiO_2), sericite

[fine-grained muscovite, $\text{KAl}_2(\text{AlSi}_3\text{O}_{10}(\text{OH})_2)$], ferroan dolomite [$\text{Ca}(\text{Mg}, \text{Fe}^{2+})(\text{CO}_3)_2$], and siderite (FeCO_3), but the region also hosts an abundance of calcite (CaCO_3), pyrite (FeS_2), chalcopyrite (CuFeS_2), and pyrrhotite (Fe_{1-x}S , $x = 0-0.2$) (Bennett et al., 1989; Hobbs et al., 1965). Minor gangue minerals also include the carbonates, dolomite [$\text{CaMg}(\text{CO}_3)_2$] and ankerite [$\text{Ca}(\text{Mg}, \text{Fe}^{2+}, \text{Mn})(\text{CO}_3)_2$].

Unfortunately, the CdA mining district is also known as the home to the Bunker Hill Superfund Site (Bennett, 1994). Mining practices employed until the 1960's involved disposal of mine tailings directly into the South Fork of the Coeur d'Alene River (CdAR), which were subsequently transported downstream (Rabe and Bauer, 1977; Reece et al., 1978). Consequently, mine tailings were deposited in the Main Stem of the CdAR as well as Lake Coeur d'Alene (Reece et al., 1978; Horowitz et al., 1992; Harrington et al., 1998). Dredging of the riverbed to allow for navigation routes, as well as flooding of the river, resulted in deposition of these mine tailings on the floodplain of the CdAR.

From nearly a century of mining in the CdA district, an estimated 115 million metric tons of mine

tailings were produced with about 60% of them discharged directly into the South Fork of the CdAR (Javorka, 1991). Ellis (1940) noted an absence of biota in the CdAR from the South Fork at Kellogg to the CdA Lake delta. Additionally, Ellis (1940) reported that some contaminants in the river would kill plankton within 36 hours and were lethal to fish within 72 hours. In 1968, federal and state regulations required the installation of tailings ponds within the CdA mining district in an attempt to suppress further pollution of the CdAR system (Rabe and Bauer, 1977). Although settling ponds greatly improved water quality within the South Fork and Main Stem of the CdAR, metals remained within the groundwater and river at levels toxic to aquatic organisms (Mink, 1971; Galbraith et al., 1972; Norbeck, 1974; Rabe and Bauer, 1977). Additionally, erosion of riverbanks along the South Fork of the CdAR contributes high concentrations of suspended metal-laden sediments to the river system (Ioannou, 1979). Sediments of the Main Stem of the CdAR contain elevated concentrations of Cd (22.6 mg kg^{-1}), Mn ($1,600 \text{ mg kg}^{-1}$), Pb ($4,180 \text{ mg kg}^{-1}$), and Zn ($6,650 \text{ mg kg}^{-1}$) (Reece et al., 1978). South Fork sediments are further enriched in Cd (43.3 mg kg^{-1}), Mn (8420 mg kg^{-1}), Pb (11400 mg kg^{-1}), and Zn (7550 mg kg^{-1}) (Reece et al., 1978). Further-

more, sediments of Lake CdA are highly enriched in As (201 mg kg^{-1}), Fe ($82,486 \text{ mg kg}^{-1}$), Mn ($5,953 \text{ mg kg}^{-1}$), Pb ($3,820 \text{ mg kg}^{-1}$), and Zn ($2,995 \text{ mg kg}^{-1}$) (Harrington et al., 1998; Horowitz et al., 1992).

Numerous wetlands are situated adjacent to the CdAR and lake providing a habitat for a variety of terrestrial and aquatic biota. High metal concentrations within these wetlands jeopardize the health and safety of the inhabitants. For instance, high Pb levels within aquatic plants and soils have recently been found responsible for approximately 7000 tundra swan deaths even though they spend only a few weeks in the region during spring migration (Blus et al., 1998). Contaminant dynamics within wetland ecosystems involve a complex continuum between the soil, water, plants, and microbial communities. Aquatic plants influence metal partitioning either directly by way of uptake and incorporation of metals within plant tissue or indirectly by changing the physicochemical conditions at the soil/root interface (Figure 1). During plant growth, radial oxygen diffusion and plant respiration provides enhanced microenvironments of $\text{O}_{2(g)}$ and carbonate at root surfaces (Armstrong, 1978). Consequently, upon diffusion toward the roots, metals may undergo redox transformations. Ferrous iron, for example, is readily oxidized forming ferric (hydr)oxide

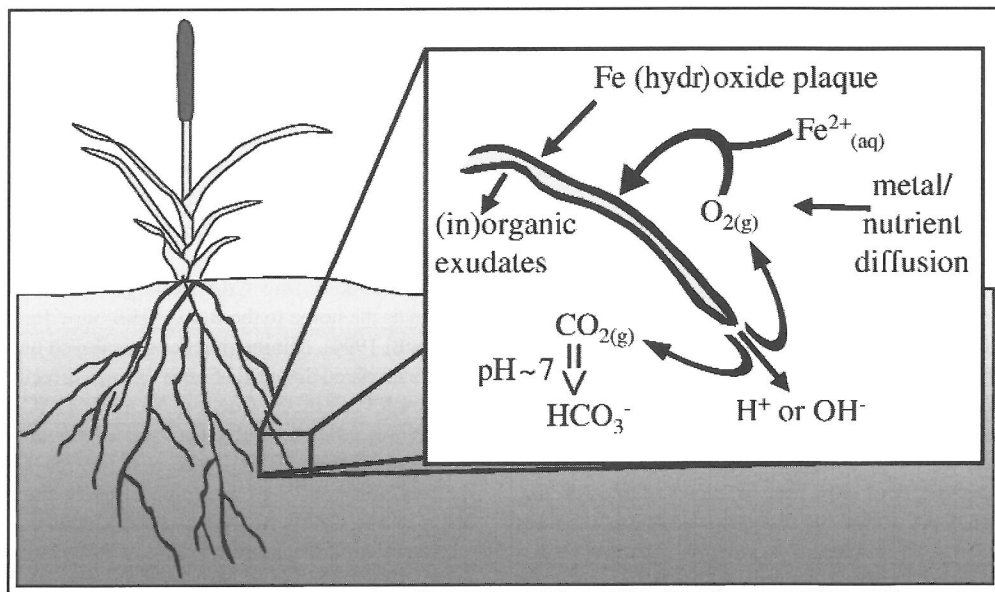


Figure 1. Simplistic schematic representation of processes occurring within the rhizosphere of aquatic plants. Oxidation zone surrounding roots ranges between ~ 1 and 4 mm (Marschner, 1995). Diagram is not to scale.

coatings (plaque) directly on root surfaces which may then provide a substrate for metal adsorption or nucleation (Bartlett, 1961; Mendelsohn and Postek, 1982; Bacha and Hossner, 1977; Chen et al., 1980; Taylor et al., 1984).

As such, metal ions may undergo a number of sorption paths within wetland soil environments: (1) precipitation or adsorption to soil minerals; (2) adsorption or complexation with soil organic matter; (3) precipitation or adsorption to root surfaces; or (4) complexation with root exudates and subsequent translocation within the plant. The partitioning and specific binding mechanisms of metals have important implications for delineating potential bioavailability and/or release of metals upon changing physicochemical conditions within aquatic environments. Accordingly, here we elucidate the partitioning and mechanisms of Mn and Zn sequestration within the soils of a natural, yet contaminated, wetland.

2. MATERIALS AND METHODS

2.1. Study Site Location and Description

The Cataldo Mission Flats constitute the floodplain of the Main Stem of the CdAR and are located approximately 30 km southeast of the city of Coeur d'Alene and 50 km east of Lake Coeur d'Alene (La Force et al., 1998) (Fig. 2). Fluvially deposited and dredged mine tailings from the Main Stem of the CdAR are situated upon the floodplain (Galbraith et al., 1972), and consequently the flats contain elevated concentrations of As, Fe, Mn, Pb, and Zn. Flooding of the CdAR results in palustrine-emergent wetlands

within the contaminated floodplain, one of which is the focus of this study and is hereinafter referred to as the Cataldo wetland (Cowardin et al., 1979). Briefly, the palustrine wetland classification includes all non-tidal wetlands situated on river floodplains or shoreward of lakes, river channels, or estuaries, which are dominated by trees, shrubs, persistent emergents, emergent mosses or lichens (Cowardin et al., 1979). In the United States, the majority of wetlands are palustrine-emergent (Cowardin et al., 1979; Fretwell et al., 1996); therefore, investigating Mn and Zn within the Cataldo wetland will have considerable implications for other mine-waste influenced wetlands. Seasonal flooding of the CdAR supplies a yearly influx of sediment and water (possibly metal-laden) to the Cataldo wetland. During winter, however, the groundwater from the wetland discharges into the low-level CdAR.

The Cataldo wetland hosts an abundance of vegetation and wildlife. Wetland inhabitants include a variety of terrestrial mammals and waterfowl. Trees in the area include alder, aspen, birch, cottonwood, willow, ponderosa pine, and white pine. The wetland accommodates a number of aquatic plant species including common cattail (*Typha latifolia*), small-fruited bulrush (*Scirpus microcarpus*), ovate spike-rush (*Eleocharis ovata*), common rush (*Juncus effusus*), common horsetail (*Equisetum arvense*) and reed canarygrass (*Phalaris arundinacea*). Four indigenous plant species vegetate ca. 95% of the wetland area: *T. latifolia* (50%), *P. arundinacea* (20%), *E. arvense* (20%), and *S. microcarpus* (5%). Isolated patches of various plant species and shrubs or unvegetated soil occupy the remaining 5% of the wetland area.

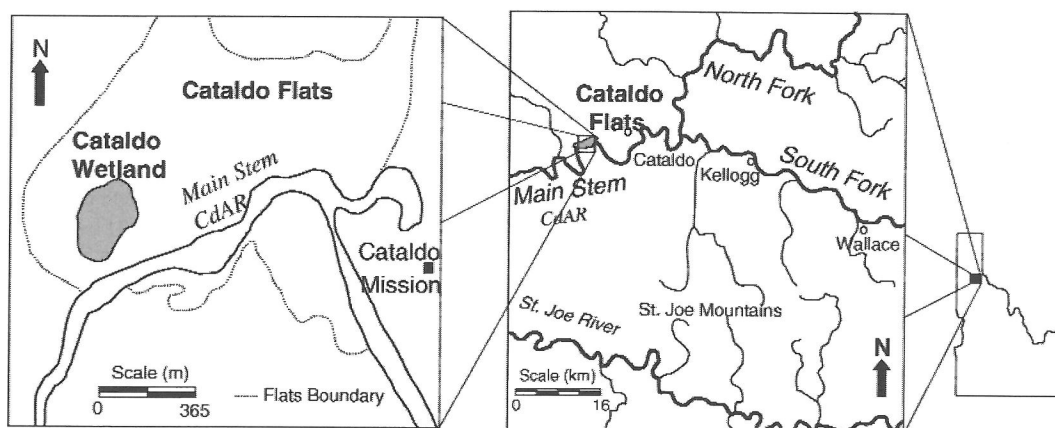


Figure 2. Location of the Cataldo Flats (right) and study site, Cataldo wetland (left).

2.2. Sample Collection and Preparation

Plant, soil, and water samples were collected in May of 1998 from the Cataldo wetland. Three samples of the four dominant plant species (*T. latifolia*, *P. arundinacea*, *E. arvense*, and *S. microcarpus*) were collected and stored on ice for transport to the laboratory. Plants were then divided into root and shoot portions and washed (lightly scrubbed) thoroughly with double-deionized water to remove any attached soil particles from the roots. Samples were dried to a constant weight at 70 °C and ground in a mill to pass a 20-mesh (0.84 mm) sieve. Plant roots used for spectroscopic analyses were collected and immediately washed, freeze-dried, and mounted on an acrylic plate and sealed with Kapton polyimide film to prevent moisture loss while minimizing x-ray absorption.

Soil samples were obtained using a 4-cm diameter PVC piston-coring device (La Force et al., 2000a). Cores collected via this procedure were then immediately capped and placed upright into a N₂-purged sample transporter (La Force et al., 2000a). Upon returning to the laboratory, the top 0-15 cm were homogenized in a N₂-purged atmosphere glovebox (Labconco, Kansas City, MO).

Membrane-separated diffusion cells (peepers) have been used extensively to monitor metal ions in solution (Brandl and Hanselmann, 1991; Carignan 1984; Carignan et al., 1985). Peepers used in this experiment were created following the procedures of La Force et al. (2000a). The peepers were placed in the wetland for two weeks, which was a sufficient time to reach equilibrium at this site (La Force et al., 2000a). In the field, aqueous samples were removed from the peepers and Eh and pH were recorded using a portable meter. Samples were then acidified with concentrated HCl and kept on ice until metal analysis 3 h later. A field blank of double deionized water with 2 drops of concentrated HCl was also run with the samples as a quality control; metal concentrations in the blank were negligible.

2.3. Total Metal Analysis

Concentrations of metal(loid)s within plant portions were determined using a wet digestion procedure consisting of nitric acid followed by successive additions of 30% hydrogen peroxide and heating. Specifically, samples (0.2 g) were digested with 4 mL of nitric acid for 24 h. Four mL of hydrogen peroxide were then added to each sample followed by heating in a digestion block (100±2°C) for 30 min. Hydrogen peroxide-heating treatments were repeated until plant residue disappeared.

Soil samples underwent total digestions using a combination of acid additions, shaking, and heating. Samples (1 g dry weight) were first digested with 5 mL of aqua regia (3:1 HCl:HNO₃ by volume) followed by shaking for 2 h. Ten mL of hydrofluoric acid were then added followed by shaking for an additional 2 h and heating in a digestion block (100±2 °C) for 1 h. Lastly, 2 g of concentrated boric acid were added to each sample and shaken for 1 h. Samples were then centrifuged and supernatants were passed through a 0.2-µm filter.

Supernatants from plant and soil digestions, as well as water samples, were analyzed for Mn and Zn via inductively coupled plasma-optical emission spectroscopy (Thermo Jarrell Ash IRIS ICP-OES; Franklin, MA) with a 10% accuracy range and quality control was checked every 15 samples. Detection limits were defined as 3σ (where σ is the standard deviation) of 5 blanks (Klesta and Bartz, 1996). Detection limits were: Mn 0.01 mg L⁻¹ and Zn 0.02 mg L⁻¹.

2.4. Soil/Root Density Calculations

Soil and root densities were determined for use in Mn and Zn mass calculations. Six cores were extracted within the four dominant plant areas of the wetland. Cores were 15 cm in length and contained a soil volume of 68.7 cm³. Bulk density of the soil was determined by typical procedures (USDA, 1996). The mineral density was determined after loss on ignition (USDA, 1996). Similarly, root densities were determined by air drying the soil, removing the readily visible root fractions, and then following the above-described method for mineral fraction determinations. It is important to note that the root density may be underestimated due to the difficulty in isolating and removing fine root hairs; hence metal concentrations associated with the root fraction are conservative and may be much larger.

2.5. Microscopic/Spectroscopic Techniques

In order to determine the bulk mineralogy of Mn and Zn in the solid-phase, x-ray absorption spectroscopy [near-edge structure (XANES) spectroscopy and extended x-ray absorption fine structure (EXAFS) spectroscopy] were performed on beamlines IV-1, IV-2, and IV-3 (beamline IV is an 8 pole wiggler) at the Stanford Synchrotron Radiation Laboratory (SSRL), running under dedicated conditions. The ring operated at 3 GeV with a current ranging from ≈100 mA to ≈50 mA. Energy selection was accomplished using a Si (220) monochromator typically with an unfocused beam. De-

pending on the beamline, higher-order harmonics were either eliminated by a harmonic rejection mirror or by detuning ~ 60% for Mn and 30% for Zn. Absorption spectra were recorded by fluorescent x-ray production using a wide-angle ionization chamber (Lytle et al., 1984) for model compounds or a 13-element Ge semiconductor detector for unknown samples. A Cr (for Mn) and Cu (for Zn) filter along with Soller slits were used to minimize the effects of scattered primary radiation when using the fluorescent ionization chamber. Incident and transmitted intensities were measured with in-line ionization chambers. The energy range studied was -200 to +500 eV about the K-edge of Mn (6539 eV) and -200 to +1000 eV about the K-edge (9659-eV) of Zn. Each scan was calibrated internally by placing elemental foil between the second and third in-line ionization chambers. Between 5 and 10 individual spectra were averaged for each sample. The reported Mn EXAFS spectra were obtained at 11 K to reduce the thermal disorder of the specimen; all other spectra were collected at ambient temperature and pressure.

X-ray absorption spectra of model Mn compounds used for analysis included feitknechtite (β -MnOOH), bixbyite (α -Mn₂O₃), rhodochrosite (MnCO₃), manganite (γ -MnOOH), pyrolusite (β -MnO₂), and birnessite (δ -MnO₂). Manganese standards of pyrolusite, bixbyite, and rhodochrosite were purchased from Fischer Scientific, Strem Chemicals, and Alpha Aesar, respectively. Hausmanite, feitknechtite, and manganite were synthesized from procedures modified after Hem and Lind (1983), Hem et al. (1982), and Bricker (1965) as described in Fendorf et al. (1999a); birnessite was made following procedures of Fendorf and Zasoski (1992). The purity of all mineral standards was checked using x-ray diffraction.

Spectra were analyzed using WinXAS (XANES) and EXAFSPAK (EXAFS) software (George, 1993). Fluorescence spectra were background-subtracted and the atomic absorption was normalized to unity. Isolation of backscattering contributions was accomplished by fitting a spline function to the absorption envelope and then subtracted it from the spectra. The isolated function was then transformed from units of eV to \AA^{-1} to produce the EXAFS function $[\chi(k)]$ where k (\AA^{-1}) is the photoelectron wave vector, which was then weighted by k^3 . The $\chi(k)$ spectrum was Fourier-transformed to produce the radial structure function (RSF) in R-space (\AA). First-shell peaks were individually isolated and backtransformed (Fourier-filtered). Fourier-filtered (FF) spectra were then fit with the predicted function in which the coordination number (CN), interatomic distance (R), and disorder (σ^2) were varied

to give the best fit between the experimental and predicted spectra.

X-ray microprobe and x-ray fluorescence microtomography (FCMT) were used to determine spatial distributions and associations of Mn and Zn on and within *P. arundinacea* roots. Microtomography scans were collected on beamline (undulator) 13-ID-C at the Advanced Photon Source, Argonne National Laboratory. For FCMT, the intact (unaltered) root was mounted on the rotation axis of a x-y-theta stepping motor stage. Fluorescence data were collected with a solid-state energy dispersive x-ray detector which allows multiple elements to be detected simultaneously. The FCMT data were obtained by translating the root through the x-ray beam and collecting fluorescence at each 2-micron step. At each position, the fluorescence signal from a given element is proportional to the integrated number of atoms of that element along the ray transected by the beam. The sample is then rotated by 0.5 about the vertical axis and the line scan repeated. The process is continued until the particle has been rotated through a total of 180 at the end of which a 2D plane has been sampled.

Microprobe scans were also obtained to reveal a more detailed (higher magnification) cross-sectional view of the root. Manganese and Zn were mapped simultaneously along the same transect such that direct spatial associations and distributions were ascertained. Scans were performed on beamline 10.3.2 at the Advanced Light Source Lawrence, Berkeley National Laboratory using micro-x-ray fluorescence. The ring operated at ~1.9 GeV with a current of approximately 400 mA. The beam energy was set at ~10 keV and a dual-channel semi-conductor Si(Li) detector was used for fluorescent x-ray detection. The technique involved irradiating the sample with a micron-sized beam of light of a fixed energy, then rastering the sample position to obtain an elemental distribution map over the chosen area. One channel of the detector was windowed to collect K_{α} emission from Mn and the other for Zn. The scan covers a 250 μm x 250 μm section of the root with data collection at 5- μm increments.

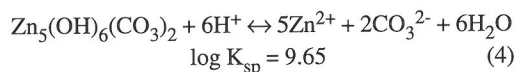
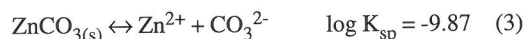
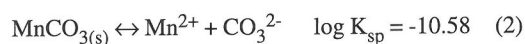
2.6. Solution Analysis and Speciation

Water samples obtained from the peepers were analyzed for Mn and Zn via inductively coupled plasma-optical emission spectroscopy (Thermo Jarrell Ash IRIS ICP-OES; Franklin, MA) with a 10% accuracy range and quality control was checked every 15 samples. Detection limits were defined as 3σ (where σ is the standard deviation) of 5 blanks (Klesta and Bartz, 1996). Detection limits were: Mn 0.01 mg L^{-1} and Zn 0.02 mg L^{-1} .

Saturation indices (SI) were obtained to determine if the solution is oversaturated, undersaturated, or in equilibrium with the observed solid phases as follows:

$$SI = \log(IAP/K_{sp}) \quad (1)$$

where K_{sp} is the solubility constant for the solid-phase and the ion activity product (IAP) is the total activity of the ions that comprise the solid-phase. Saturation indices for Mn and Zn phases were calculated using the computer code MINTEQA2. The following equations and solubility constants were used for saturation-index computations (Johnson, 1982; Johnson et al., 1992; Schindler et al., 1969):



For the soil analysis, a pH value of 7.05 and peak concentrations for Mn (6 mg kg^{-1}) and Zn (0.03 mg kg^{-1}) were utilized in calculations. Although carbonate concentrations were not directly measured in the field, carbonate values in anaerobic soils are typically an order of magnitude higher than atmospheric and were thus set at $P_{CO_2} = 10^{-2.5} \text{ atm}$.

3. RESULTS

3.1. Metal Budgets

The bulk wetland soil pH is circumneutral with values decreasing slightly with depth (Table 1). Similarly, Eh values indicate a decreasing soil redox potential with depth and the presence of reducing conditions. Rhizosphere pH and Eh values were not obtained on plant samples due to the difficulty in performing micro-scale field measurements. However, rhizosphere pH values may differ by 2 units from the bulk soil pH depending on plant and soil characteristics (Marschner, 1995).

Table 1. Water chemistry as a function of depth.*

Depth cm	Eh mV	pH	Mn mg L ⁻¹	Zn
-10	410	7.29	0.17	nd
-5	325	7.16	0.10	nd
0	222	7.05	6.0	nd
5	213	6.94	0.47	0.03
10	219	6.81	1.0	nd
15	200	6.94	0.22	nd

* nd = not detected

Within wetland ecosystems, Mn and Zn may accumulate within the soil, solution, and vegetation. The partitioning of Mn and Zn within these fractions is reported in Tables 1 and 2. Solution concentrations of Mn and Zn are minimal within a range of 10 cm above and 15 cm below the soil/water interface (Table 1). Dissolved Mn concentrations peak at 6 mg L^{-1} at the soil/water interface while aqueous Zn is only detected at a depth of 5 cm (0.03 mg L^{-1}). In contrast, Mn and Zn concentrations are elevated in the soil and plant fractions (both root and shoot portions) (Table 2). Total concentrations of Mn and Zn within the soil did not differ significantly throughout the various regions of the wetland and hence soil concentrations are represented as a wetland average. Concentrations of Mn and Zn with plant roots are generally comparable with the soil and, at times, exceed those of the soil. Additionally, total Mn and Zn concentrations are on average higher in the roots relative to the shoot (aerial) portions.

To obtain a better understanding of the relative contribution of metal abundance within the wetland subsurface (excluding plant shoots), Mn and Zn mass calculations were obtained using soil and root densities, metal concentrations, and wetland area (Table 3). The Cataldo wetland's area is $\sim 78,200 \text{ m}^2$, with four plant species (*T. latifolia*, *P. arundinacea*, *E. arvense*, and *S. microcarpus*), accounting for ca. 95% ($\sim 74,290 \text{ m}^2$) of the total area. Since the soil and plant samples were extracted to a 0.15-m depth, we consider a wetland volume of $11,730 \text{ m}^3$ and the four dominant plant species stands comprise

Table 2. Manganese and zinc concentrations within the wetland soil and plants.*

	Roots		Shoots		Soil	
	Mn	Zn	Mn	Zn	Mn	Zn
	mg kg ⁻¹					
					1600	1300
<i>T. latifolia</i>	790	350	3400	86		
<i>P. arundinacea</i>	1500	950	1200	510		
<i>E. arvense</i>	1900	300	1800	250		
<i>S. microcarpus</i>	1000	1300	1500	250		

* values reported as mean of triplicate analysis, relative standard deviations are within 10%

11,144 m³. Using the fractional abundance of each plant species, the volume of soil within each plant stand was calculated. Within the top 15 cm, the corresponding soil mineral densities range from 0.42 to 0.50 g cm⁻³ and root densities from 0.05 to 0.06 g cm⁻³. Soil and root densities were consistent throughout individual plant stand areas and thus reflect a considerable degree of homogeneity within plant species.

Using the aforementioned densities and volumes, the mass of Mn and Zn within the soil and four plant

species were obtained (Table 3). Manganese associated with the roots of the different plant species is remarkably similar, excluding *S. microcarpus*. Zinc, on the other hand, is lower in both in *S. microcarpus* and *E. arvense* relative to *T. latifolia* and *P. arundinacea*. Within the top 15 cm of the Cataldo wetland, 7,840 kg of Mn are associated with the soil and 707 kg with plant roots. Similarly, 6,360 kg of Zn are affiliated with the soil fraction and 319 kg with roots. Plant roots thus sequester ca. 8% of Mn and 5% of Zn sequestration with this ecosystem.

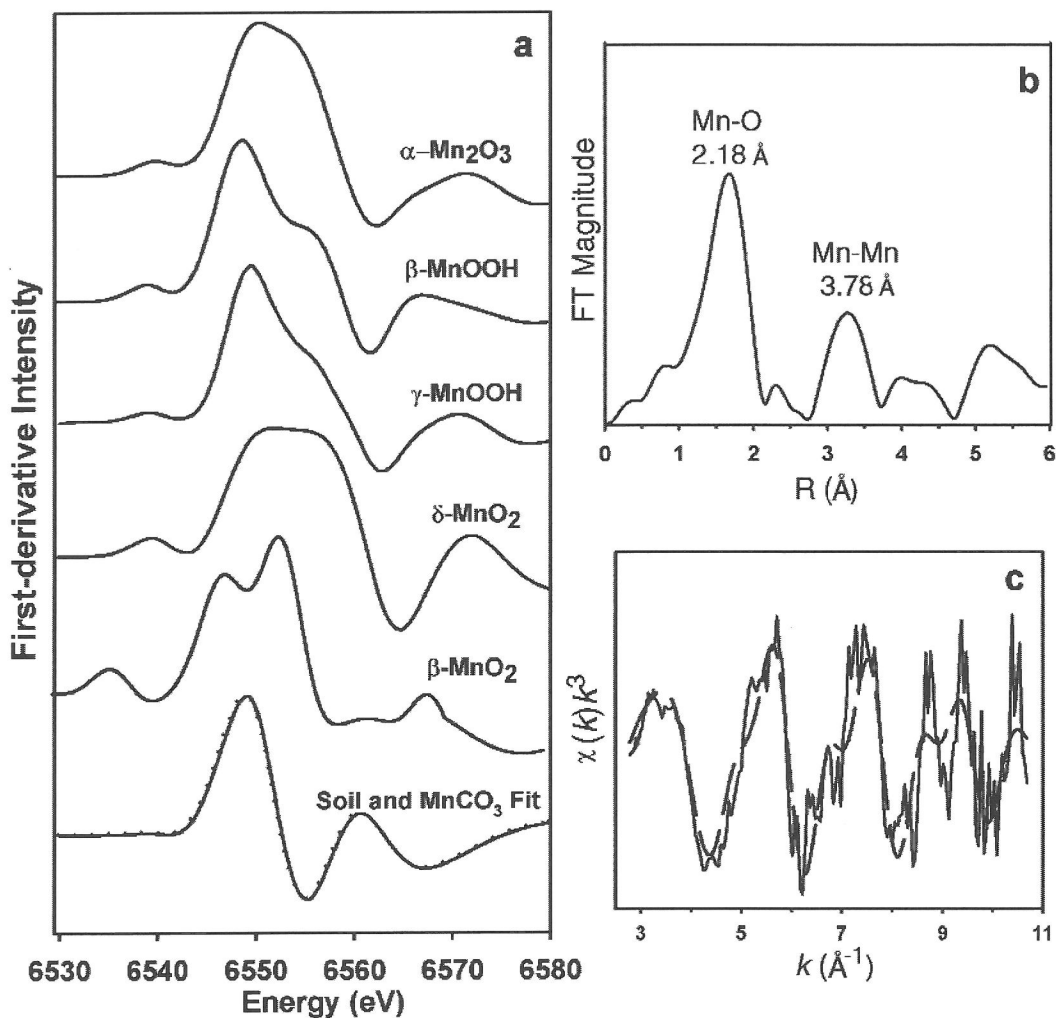


Figure 3. Spectroscopic analyses of soil Mn illustrated by (a) XANES spectra for various Mn standard compounds and wetland soil, (b) Fourier-transformed EXAFS spectrum, and (c) normalized k³-weighted EXAFS spectra. Theoretical fit is indicated by the dashed line. The Fourier-transform spectrum is not phase-shift corrected and thus peak positions are less than true interatomic distances.

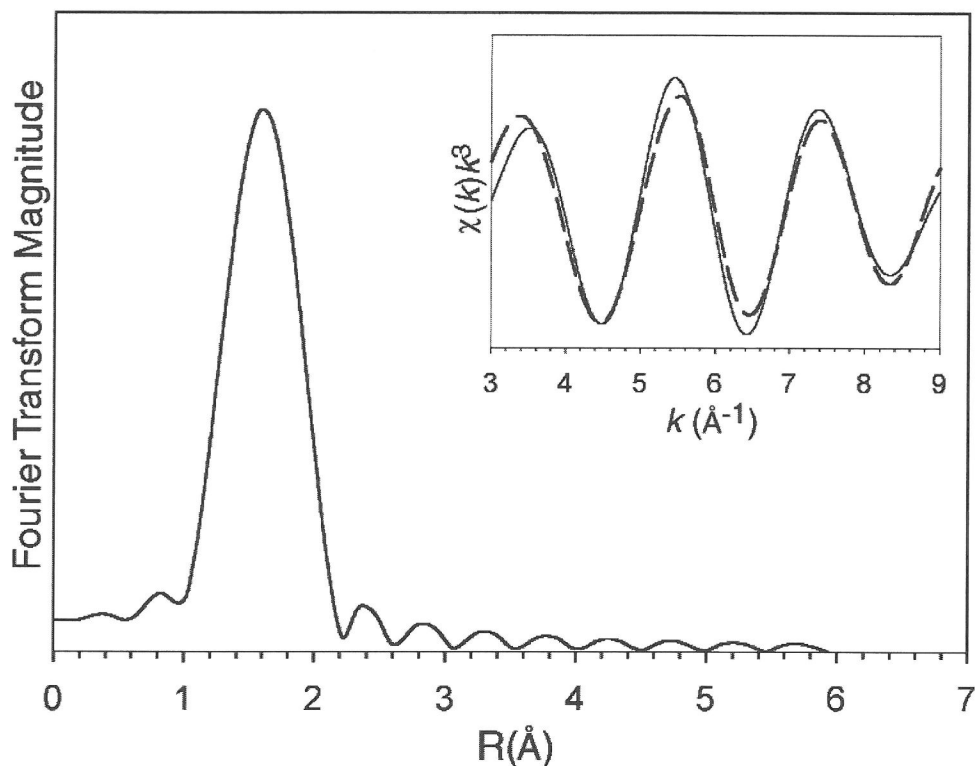


Figure 4. Fourier-transformed (FT) spectrum of Zn in the soils resulting in a radial structure function in real space (Å). Fourier-transform is not phase-shift corrected and thus peak positions are less than true interatomic distances. Inset represents the k^3 -weighted, Fourier-filtered first shell (Zn-O) from the FT spectrum illustrating the theoretical fit (dotted line) to the experimental curve (solid line).

Table 3. Manganese and Zn budgets within the wetland.

Plant Species	Abundance* %	Volume [¶] m ³	Density g cm ⁻³		Mass (kg) [†]			
					Mn		Zn	
			Soil	Roots	Soil	Roots	Soil	Roots
<i>T. latifolia</i>	50	5865	0.42	0.05	3900	230	3200	100
<i>P. arundinacea</i>	20	2346	0.50	0.06	1900	210	1500	140
<i>E. arvense</i>	20	2346	0.42	0.05	1600	230	1300	35
<i>S. microcarpus</i>	5	587	0.47	0.06	440	37	360	44
Total [‡]	95	11144			7840	707	6360	319

* abundance based on relative proportions of different plants within wetland

[¶] volume calculated from relative abundance and total wetland volume (11,730 m³) to a 15-cm depth

[†] mass reported as mean of 6 samples; relative standard deviations are within 10%

[‡] remaining 5% = unvegetated and mixed plant and shrub regions

3.2. Speciation of Mn and Zn in Soils

The positioning of the main absorption edge in the XANES spectrum and corresponding first-derivative curve can be used to differentiate Mn oxidation states in soil (higher oxidation states occur at greater ener-

gies) (Manceau et al., 1992; Schulze et al., 1995; Friedl et al. 1997; Fendorf et al., 1999b; Ressler et al., 2000). For example, Mn(II) and Mn(IV) are separated by ~4 eV in their first-derivative XANES spectra. Manganese carbonate has a lower pre-edge intensity and absorption edge position, owing to its six-fold co-

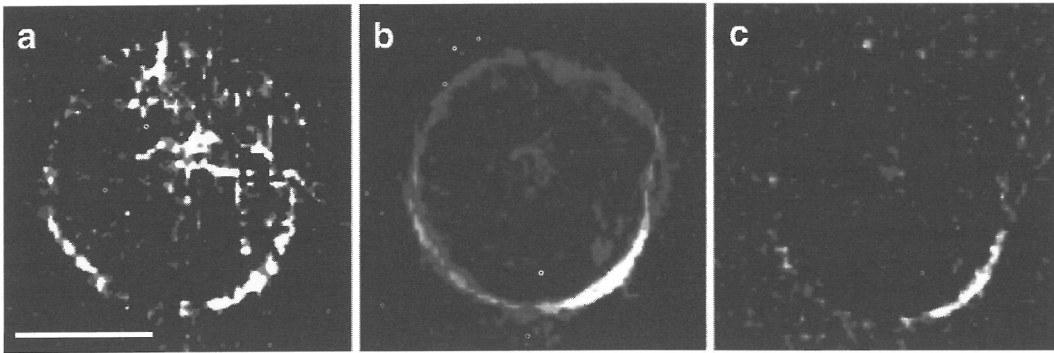


Figure 5. Metal distributions on and within *P. arundinacea* roots. Microtomographic images of (a) Mn (b) Zn and (c) Ca. Scale bar represents 300 μm .

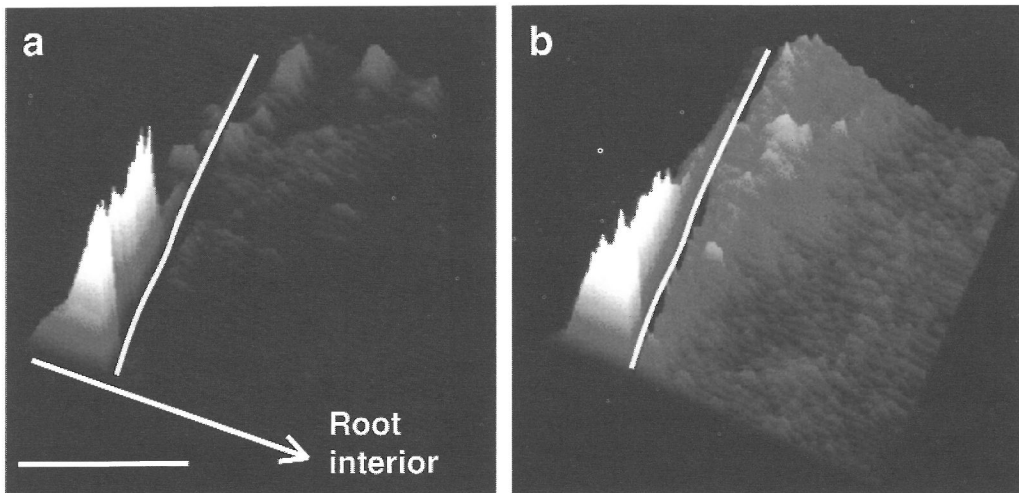


Figure 6. Higher magnification x-ray microprobe image of (a) Mn and (b) Zn along a transect from the root center to the exterior of the plaque (scale bar represents 50 μm). Preserved roots were sliced in half longitudinally to reveal a cross-sectional view. The yellow line represents the root epidermis and relative elemental concentrations increase with color brightness.

ordination and lower oxidation state than higher valent Mn (hydr)oxides (Fig. 2) (Manceau et al., 1992; Schulze et al., 1995). Quantitative analysis of our unknown soil samples collected from the wetland revealed that pre-edge peak amplitudes and main absorption edges were consistent in all Mn samples and are consistent with the rhodochrosite spectrum. Thus, Mn(II) is the dominant solid-phase oxidation state and appears to have a rhodochrosite-like structure. In addition, linear combination fitting of the un-

known Mn species were best reproduced using the rhodochrosite spectrum (Fig. 3).

We used EXAFS spectroscopy to confirm the local structure of Mn in the solids as rhodochrosite-like phases. The Fourier transformed and unfiltered k^3 -weighted $\chi(k)$ EXAFS function are shown in Fig. 3 with associated spectra predicted for rhodochrosite. Predicted spectra were calculated using published values for the first two Mn shells in rhodochrosite (Effenberger et al., 1981; Friedl et al., 1997). Unfor-

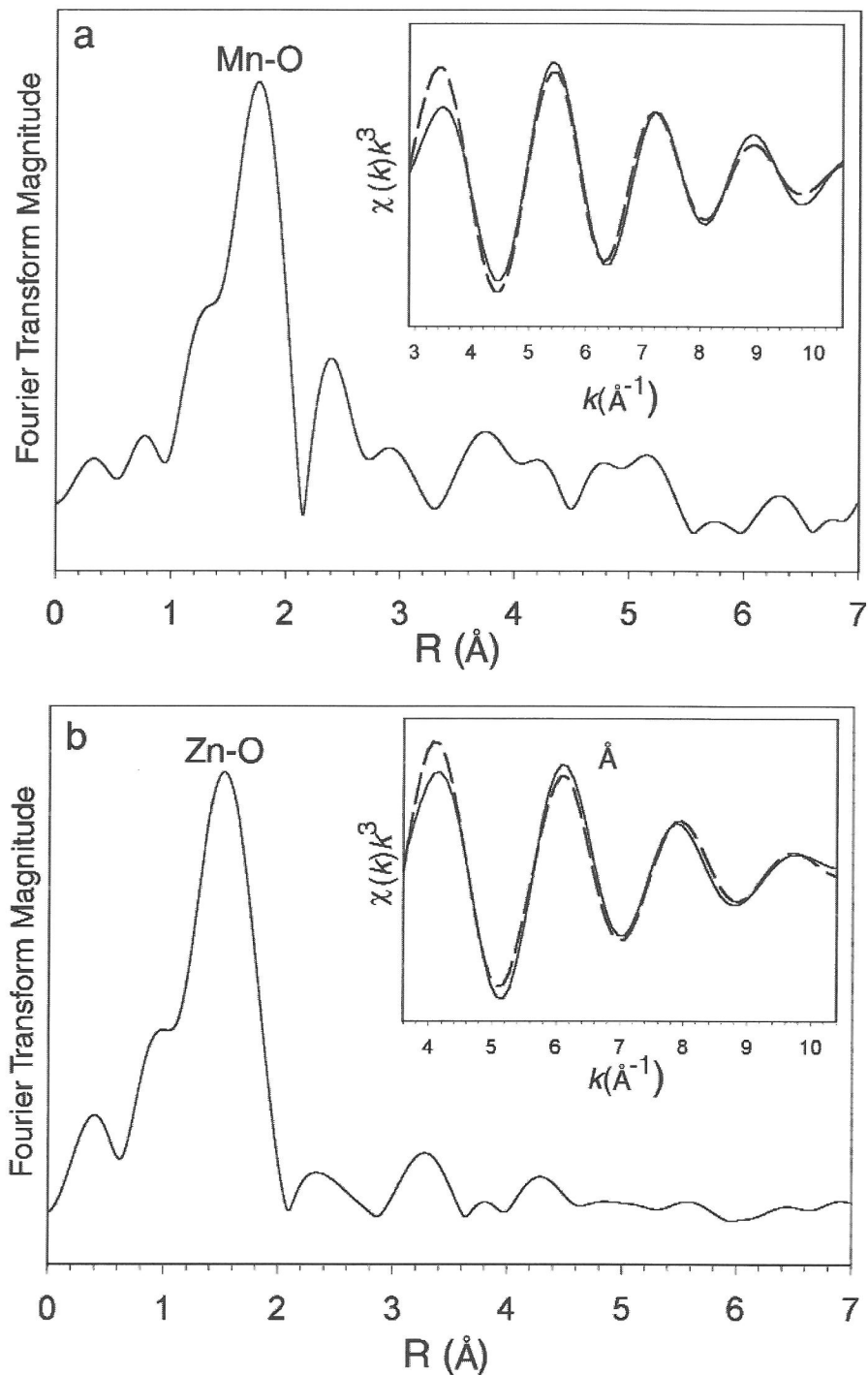


Figure 7. Fourier-transformed (FT) spectra of (a) Mn and (b) Zn resulting in a radial structure function in real space (Å). Fourier-transforms are not phase-shift corrected and thus peak positions are less than true interatomic distances. Insets represent the k^3 -weighted, backtransformed first shells [(a) Mn-O and (b) Zn-O] from the FT spectra illustrating the theoretical fits (dotted lines) to the experimental curve (solid lines).

unately, it is difficult to decipher whether the manganese carbonate is a pure species or a solid-solution.

The coordination environment for Zn within the soil was also determined using EXAFS spectroscopy (Fig. 4). Zinc is octahedrally coordinated by oxygen with a Zn-O radial distance of 2.11 Å corresponding to a smithsonite-like (ZnCO_3) phase or Zn-substituted CaCO_3 (Effenberger et al., 1981; O'Day et al., 1998). Although second-shell radial distances could be used to differentiate these two possibilities, we could not resolve second shells sufficiently to allow for this distinction.

3.3. Spatial Distribution and Speciation of Mn and Zn on Plant Roots

On the surface of *P. arundinacea* roots, microtomographic images illustrate that Mn and Zn are elevated in discrete zones on the exterior of the epidermis whereas, in contrast, concentrations diminish in areas adjacent to these zones. Zinc and Mn are strongly correlated aside from the root interior where Mn concentrations are considerably higher (Fig. 5a,b). Additionally, Ca levels are elevated at sites of Zn and Mn precipitation (Fig. 5c). A more detailed (higher magnification) depiction of Mn and Zn distributions further illustrates the strong correlation between Mn and Zn (Fig. 6a,b). Moreover, a nodular morphology of the Mn/Zn precipitates is portrayed. Scans were performed on extensive portions of various roots and the results were consistent with those illustrated in Figures 5 and 6.

The local coordination environment of Mn and Zn, determined using EXAFS spectroscopy (Fig. 7), reveals that Mn is octahedrally coordinated by oxygen. Similar to the soil results, the Mn-O interatomic distance is 2.20 Å, which is in close agreement with published values (2.19 Å) for rhodochrosite (MnCO_3) (Effenberger et al., 1981; Friedl et al., 1997). In contrast, the first shell for Zn is a composite of three distinct sites (2 octahedral and 1 tetrahedral) having an average of four different interatomic distances (2.08, 2.06, 2.15, and 1.96 Å). The Zn-O(H) distances correspond to published values for hydrozincite [$\text{Zn}_5(\text{OH})_6(\text{CO}_3)_2$] (Ghose, 1964; O'Day et al., 1998). Accordingly, on the basis of the EXAFS analyses, the discrete nodules observed on *P. arundinacea* roots are composed of Mn and Zn carbonate phases.

3.4. Geochemical Modeling of Mn- and Zn-Carbonate Phases

MINTEQA2 was used to determine if the pore waters were saturated with respect to the observed carbonate phases within the soil and on plant roots. The

bulk pore water is near equilibrium ($\text{SI} \approx -0.193$) with respect to rhodochrosite but undersaturated ($\text{SI} \approx -3.02$) with respect to smithsonite. It is important to note that the K_{sp} values assume a pure species yet as mentioned previously, we could not differentiate between a pure smithsonite species or a Zn-substituted Ca carbonate phase. Alternatively, considering that wetland water levels are beginning to decline at this point in time, Zn phases may be in a transitional period and it may therefore be feasible that smithsonite is dissolving.

It is well-established that steep gradients in nutrient concentrations, pH, redox potential, and carbonate values occur at the soil-root interface (Marschner, 1995). Within the rhizosphere, carbonate concentrations can approach 5 mmol L^{-1} , while pH values can be 2 units greater and nutrient concentrations several times higher than those in bulk solution (Bedford et al., 1991; Marschner, 1995; Linehan et al., 1989). Although it is difficult to predict the chemical environment within the rhizosphere, if we consider merely a 1 unit pH increase (8.05) and Zn concentrations three times that in the bulk solution, the pore water is in equilibrium with hydrozincite ($\text{SI} \approx 0$). Furthermore, Zn is an essential nutrient to plants and thus more realistic Zn concentrations are most likely greater than 5 times that in the soil; given such a concentration, saturation with respect to hydrozincite would be exceeded. Similarly, Mn concentrations at the root surface will be several times higher than within the bulk solution. Considering that the pore water within the bulk solution is in equilibrium with rhodochrosite, the more favorable conditions within the rhizosphere will promote rhodochrosite saturation.

4. DISCUSSION

The partitioning of Mn and Zn within the Cataldo wetland is dominantly between the mineral fraction and plant roots while solution concentrations are negligible. Concentrations of Mn and Zn associated with roots vary among plant species; however, at times, root concentrations are roughly equivalent to those of the soil. Yet, owing to higher soil densities, the mass contributions are ≥ 10 -fold higher in the mineral fraction relative to roots of all plant species. Nevertheless, root surfaces are providing an essential substrate for metal nucleation accounting for 8% of Mn and 5% of Zn sequestration with the wetland soils.

Spectroscopic analyses reveal the dominance and significance of carbonate ligands in precipitation, and subsequent sequestration, of Mn and Zn. XAS data reveal that a rhodochrosite-like phase is the dominant Mn phase within the soil and on the surface of *P. arundinacea* roots. Similar to Zn, first-shell data

cannot differentiate between a pure rhodochrosite or a Ca-Mn carbonate solid-solution. On root surfaces, however, Ca exhibits a strong correlation with Mn and Zn and may therefore suggest that Ca carbonate (CaCO_3) is in some manner associated with Mn and Zn deposition on root surfaces, and perhaps within the soil as well.

Zinc is also bound by carbonate ligands, yet the phase varies from smithsonite-like in the soil to its hydrated derivative hydrozincite [$\text{Zn}_5(\text{OH})_6(\text{CO}_3)_2$] on the root surface. Smithsonite formation is very slow under surface temperatures and pressures; hydrozincite, on the other hand, is formed over a wide range of $\text{CO}_{2(g)}$ partial pressures (Zachara et al., 1989a). Structural dissimilarities among rhodochrosite and hydrozincite impede epitaxial growth and subsequent solid-solution (Zachara et al., 1989a). Thus, the probable association between the rhodochrosite-like and hydrozincite-like phases within the root-borne nodules is as a mixture of discrete precipitate domains.

On the basis of our analyses, Zn is incorporated into a smithsonite-like (ZnCO_3) phase and/or as Zn-substituted CaCO_3 within the soil. Zinc may initially adsorb on calcite where it may be incorporated into the CaCO_3 crystal lattice or nucleate as a smithsonite precipitate (Zachara et al., 1989b; Reeder, 1996; Zachara et al., 1991). Smithsonite formation, albeit slow, may be induced in an elevated carbonate environment or by initial nucleation onto CaCO_3 surfaces (surface catalysis). Alternatively, if hydrozincite is metastable, it may initially precipitate either in the presence or absence of CaCO_3 , followed by its transformation into a smithsonite-like phase; however, the time-dependent feasibility for such conversion is unknown (Zachara et al., 1989a; Botcher, 1995). In general, Zn precipitation may involve a single phase or a convolution of carbonate phases within the soil.

Although only Spring results are presented, Mn concentrations, speciation, and structural environments are equivalent throughout the year (La Force et al., 2000b). Correspondingly, when wetland water levels decline and the soils become aerated, XAS analyses of the roots and soil still reveal Mn carbonates as the dominant phases (La Force et al., 2000b). However, sequential selective extractions of the wetland soils indicate that the concentration and proportion of Mn-carbonates relative to other Mn phases varies an order of magnitude throughout the year (La Force et al., 2000b). Conversely, the structural environment of Zn within the soil varies significantly throughout a year with carbonate phases dominating during Spring when water levels and microbially respired carbonate levels are elevated (Bostick et al., 1999). As water levels decline, however, Zn oxide

phases dominate the partitioning of Zn. The data suggest, therefore, that the presence and dominance of Mn and Zn carbonate phases is primarily a consequence of secondary precipitation rather than residual ore deposition. Zinc on the root surface, however, remains associated with a carbonate phase (hydrozincite) throughout the year and thus denotes a more consistent environment in the rhizosphere for carbonate formation and stability (data not shown).

The strong correlation between Mn and Zn and their morphology are illustrated by the x-ray microprobe and microtomography images of *P. arundinacea* roots. Manganese and Zn exist as discrete carbonate "nodules" on the root surface with concentrations diminishing in areas adjacent to these clusters. Due to the structural dissimilarity of rhodochrosite and hydrozincite, these phases seemingly exist in isolated regions within the nodule. Roots, therefore, provide a substrate for carbonate nucleation, as well as stimulate an enhanced carbonate microenvironment by way of root and/or microbial respiration. Owing to the structural similarity between soil and root-associated carbonate phases, it may be speculated that a similar nodular morphology exists on mineral surfaces with surface defect sites providing the site of nucleation.

5. CONCLUSIONS

Past mining practices have jeopardized environmental quality in many regions, including the Coeur d'Alene district, by introducing toxic metals to the water, soils, and biota. Public health relies on the immobilization of such metals to restrict their introduction into drinking water and food chains. Wetlands provide a "sink" for metals, yet the mechanisms of metal sequestration within these unique ecosystems are not well understood. Accordingly, we have shown in this study the dominant role of carbonates in Mn and Zn sequestration within a natural, mine-waste impacted wetland.

Metal budgets indicate that the soil mineral fraction and the surface of plant roots are the dominant players in Mn and Zn retention, while dissolved concentrations are negligible. Manganese and Zn are highly correlated within the soil and on the surface of plant roots, occurring as carbonate phases. On plant roots, and possibly within the soil, Mn, Zn, and Ca carbonate nodular deposits occur at discrete sites on the surface.

Accordingly, these results have profound consequences on predicting the fate and modeling the transport of metals within anaerobic soils. In this study, we elucidate the behavior of Mn and Zn cycling in wetland ecosystems. Carbonate ligands ap-

pear to be the dominant means by which Zn and Mn are sequestered and immobilized within this wetland ecosystem, and may have a pronounced influence on metal sequestration in general. As such, carbonate precipitation of metals within the soil as well as at the soil/root interface must be considered when implementing remediation strategies, such as phytoremediation and constructed wetlands.

Acknowledgements—We gratefully acknowledge the staff of the Advanced Photon Source, Argonne National Laboratory, specifically Matt Newville for fluorescence microtomography analyses. We also thank Stanford Synchrotron Radiation Laboratory and Lawrence Berkeley National Laboratory for granted beamtime and technical assistance. This research was supported by the Exploratory Research Program of the U.S. EPA.

Editorial handling: Scott A. Wood

REFERENCES

- Armstrong W. (1978) Root aeration in the wetland condition. In *Plant Life in Anaerobic Environments* (eds. D.E. Hook and R.M.M. Crawford) Ann Arbor Science, Michigan pp. 269-298.
- Bacha R. E. and Hossner L. R. (1977) Characteristics of coatings formed on rice roots as affected by iron and manganese additions. *Soil Sci. Soc. Am. J.* **41**, 931-935.
- Bartlett R. J. (1961) Iron oxidation proximate to plant roots. *Soil Science* **92**, 372-379.
- Bedford B. L., Bouldin D. R., Beliveau B. D. (1991) Net oxygen and carbon-dioxide balances in solutions bathing roots of wetland plants. *J. Ecology* **79**, 943.
- Bennett E. H., Siems P. L., and Constantopoulos J. T. (1989) The geology and history of the Coeur d'Alene Mining District, Idaho. In *Guidebook to the Geology of Northern and Western Idaho and Surrounding Area*. (eds. V. E. Chamberlain, R. M. Breckenridge, and B. Bonnicksen) Idaho Geological Survey Bulletin 28. pp. 137-156.
- Bennett E. H. (1994) A history of the Bunker Hill Superfund Site, Kellogg, Idaho. Idaho Geological Survey. Pacific Northwest Conf., Spokane, Washington.
- Blus L. J., Henny C. J., Hoffman D. J., Sileo L., and Audet D. J. (1998) Persistence of high lead concentrations and associated effects in tundra swans captured near a mining and smelting complex in northern Idaho. *Ecotoxicology* **8**, 125.
- Bostick B. C., Hansel C. M., La Force M. J., and Fendorf S. E. (1998) Zinc local structure and partitioning within a contaminated wetland. *Stanford Synchrotron Radiation Laboratory 1998 Activity Report*. pp. 391-394.
- Bottcher M. E. (1995) The formation of rhodochrosite-smithsonite ($\text{MnCO}_3\text{-ZnCO}_3$) solid solutions at 5°C. *Mineral. Mag.* **59**, 481-488.
- Brandl H. and Hanselmann K. W. (1991) Evaluation and application of dialysis porewater samplers for microbiological studies at sediment-water interfaces. *Aquatic Sci.* **53**, 54-73.
- Bricker O. (1965) Some stability relations in the system $\text{Mn-O}_2\text{-H}_2\text{O}$ at 25° and one atmosphere total pressure. *Amer. Miner.* **50**, 1296-1355.
- Carignan R. (1984) Interstitial water sampling by dialysis: Methodological notes. *Limnol. Ocean.* **29**, 667-670.
- Carignan R., Rapin F., and Tessier A. (1985) Sediment pore-water sampling for metal analysis: A comparison of techniques. *Geochim. Cosmochim. Acta* **49**, 2493-2497.
- Chen C. C., Dixon J. B., and Turner F. T. (1980) Iron coatings on rice roots: Mineralogy and quantity influencing factors. *Soil. Sci. Soc. Am. J.* **44**, 635-639.
- Cowardin L. M., Carter V., Golet F. C., and LaRoe E. T. (1979) Classification of wetland and deepwater habitats of the United States. *U.S. Fish and Wildlife Service Report FWS/OBS-79/31*, 131 p.
- Effenberger H., Mereiterý K., and Zemanyý J. (1981) Crystal structure refinements of magnesite, calcite, rhodochrosite, siderite, smithsonite, and dolomite, with the discussion of some aspects of the stereochemistry of calcite type carbonates. *Zeitschrift für Kristallographie* **156**, 233-243.
- Ellis M. M. (1940) Pollution of the Coeur d'Alene River and adjacent waters by mine wastes. *U.S. Bureau of Fisheries, Special Scientific Report 1*, Washington, D.C.
- Fendorf S. E. and Zasoski R. J. (1992) Chromium(III) oxidation by delta- MnO_2 . 1. Characterization. *Environ. Sci. Technol.* **26**, 79-85.
- Fendorf S. E., Jardine P. M., Patterson R. R., Taylor D. L., and Brooks S. C. (1999a) Pyrolusite surface transformations measured in real-time during the reactive transport of Co(II)EDTA^{2-} . *Geochim. Cosmochim. Acta* **63**, 3049-3057.
- Fendorf S. E., Jardine P. M., Taylor D. L., Brooks S. C., and Rochette E. A. (1999b) Auto inhibition of oxide mineral reductive capacity toward Co(II)EDTA . In *Mineral-water interfacial reactions kinetic and mechanisms*. (eds. D.L. Sparks and T.J. Grundl). ACS Symposium Series 715, Washington, DC.
- Fretwell J. D., Williams J. S., and Redman P. J. (1996) National water summary on wetlands resources. *USGS Water-Supply Paper 2425*.
- Friedl G., Wehrli B., and Manceau A. (1997) Solid phase in the cycling of manganese in eutrophic lakes: New insights from EXAFS spectroscopy. *Geochim. Cosmochim. Acta* **61**, 275-290.
- Galbraith J. H., Williams R. E., and Siems P. L. (1972) Migration and leaching of metals from old mine tailings deposits. *Groundwater* **10**, 33-44.
- George G. N. (1993) EXAFSPAK. Stanford Synchrotron Radiation Laboratory.
- Ghose S. (1964) The crystal structure of hydrozincite, $\text{Zn}_6(\text{OH})_6(\text{CO}_3)_2$. *Acta Crystall.* **17**, 1051-1057.
- Harrington J. M., La Force M. J., Rember W. C., Fendorf S. E., and Rosenzweig R. F. (1998) Phase associations and mobilization of iron and trace elements in Coeur d'Alene Lake, Idaho. *Environ. Sci. Technol.* **32**, 650-656.
- Hem J. D. and Lind C. J. (1983) Non-equilibrium models for predicting forms of precipitated manganese oxides. *Geochim. Cosmochim. Acta* **47**, 2037-2046.
- Hem J. D., Roberson C. E., and Fournier R. B. (1982) Stability of beta MnOOH and manganese oxide deposition from springwater. *Water Resources Res.* **18**, 563-570.
- Hobbs S. W., Griggs A. B., Wallace R. E., and Campbell A. B. (1965) Geology of the Coeur d'Alene district, Shoshone County, Idaho. *U.S. Geological Survey Professional Paper 478*, 1-28.
- Horowitz A. J., Elrick K. A., and Cook R. B. (1992) Effect of mining-related activities on the sediment-trace element geochemistry of Lake Coeur d'Alene, Idaho, USA—Part 1. *U.S. Geological Survey Open-File Report 92-109*.
- Ioannou C. (1979) Distribution, transport and reclamation of abandoned mine tailings along the channel of the South

- Fork of the Coeur d'Alene River and Tributaries, Idaho. M.S. thesis, University of Idaho.
- Javorka E. (1991) Lake water quality assessment Coeur d'Alene Lake, Benewah and Kootenai Counties, Idaho. Coeur d'Alene Basin Interagency Group, Coeur d'Alene Tribe of Idaho, Coeur d'Alene Subagency, Plummer, Idaho. p. 42.
- Johnson K. S. (1982) Solubility of rhodochrosite (MnCO_3) in water and seawater. *Geochim. Cosmochim. Acta* **46**, 1805-1809.
- Johnson J. W., Oelkers E. H., and Helgeson H. C. (1992) SUPCRT92: A software package for calculating the standard molal thermodynamic properties of minerals, gases, aqueous species, and reactions from 1-bar to 5000-bar and 0° to 1000°C. *Comput. Geosci.* **18**, 899-947.
- Klesta E. J. Jr. and Bartz J. K. (1996) Quality assurance and quality control. In *Methods of Soil Analysis. Part 3. Chemical Methods* (ed. D.L. Sparks). SSSA ASA, Madison WI. pp. 19-49.
- La Force M. J., Hansel C. M., and Fendorf S. E. (2000a) Constructing simple wetland sampling devices. *Soil Sci. Soc. Am. J.* **64**, 809-811.
- La Force M. J., Hansel C. M., and Fendorf S. E. (2000b) Seasonal transformations of manganese in a mine-waste impacted wetland. *Soil Sci. Soc. Am. J.* In press.
- La Force M. J., Fendorf S. E., Li G. C., Schneider G. M., and Rosenzweig R. F. (1998) A laboratory evaluation of trace element mobility from flooding and nutrient loading of Coeur d'Alene River sediments. *J. Environ. Qual.* **27**, 318-328.
- Linehan D. J., Sinclair A. H., and Mitchell M. C. (1989) Seasonal changes in Cu, Mn, Zn and Co concentrations in soil in the root-zone of barley (*Hordeum vulgare* L.). *J. Soil Sci.* **40**, 103-115.
- Lytle F. W., Gregor R. B., Sandstone D. R., Marques E. C., Wong J., Spiro C. L., Huffman G. P., and Huggins F. E. (1984) Measurements of soft x-ray absorption spectra with a fluorescent ion chamber. *Nucl. Instrum. Methods Phys. Res. Sect. A.* **226**, 542-548.
- Manceau A., Gorshkov A. I., and Drits V. (1992) Structural chemistry of Mn, Fe, Co, and Ni in manganese hydrous oxides: Part I. Information from XANES spectroscopy. *Amer. Miner.* **77**, 1133-1143.
- Marschner H. (1995) Mineral Nutrition of Higher Plants. Academic Press, NY.
- Mendelsohn I. A., and Postek, M. T. (1982) Elemental analysis of deposits on the roots of *Spartina alterniflora* Loisel. *Amer. J. Bot.* **69**, 904-912.
- Mink L. L. (1971) Water quality of the Coeur d'Alene River basin. M.S. thesis, University of Idaho.
- Norbeck P. M. (1974) Water table configurations and tailings distribution, Coeur d'Alene Valley, Idaho. M.S. thesis, University of Idaho.
- O'Day P. A., Carroll S. A., and Waychunas G. A. (1998) Rock-water interactions controlling zinc, cadmium, and lead concentrations in surface waters and sediments, U.S. Tri-State Mining District. 1. Molecular identification using x-ray absorption spectroscopy. *Environ. Sci. Technol.* **32**, 943-955.
- Rabe F. W. and Bauer S. B. (1977) Heavy metals in lakes of the Coeur d'Alene River Valley, Idaho. *Northwest Science* **51**, 183-197.
- Reece D. E., Felkey J. R., and Wai C. M. (1978) Heavy metal pollution in the sediments of the Coeur d'Alene River, Idaho. *Environ. Geol.* **2**(5), 289-293.
- Reeder R. J. (1996) Interaction of divalent cobalt, zinc, cadmium, and barium with the calcite surface during layer growth. *Geochim. Cosmochim. Acta* **60**, 1543-1552.
- Ressler T., Wong J., Roos J., and Smith I. L. (2000) Quantitative speciation of Mn-bearing particulates emitted from autos burning (methylcyclopentadienyl)manganese tricarbonyl-added gasolines using XANES spectroscopy. *Environ. Sci. Tech.* **34**, 950-958.
- Schindler P., Reinert M., and Gamsjäger H. (1969) Löslichkeitskonstanten und free bildungs enthalpien von ZnCO_3 und $\text{Zn}_5(\text{OH})_6(\text{CO}_3)_2$ bei 25°C. *Helvetica Chim. Acta* **52**, 2327-2332.
- Schulze D. G., Sutton S. R., and Bajt S. (1995) Determining manganese oxidation-state in soils using x-ray absorption near-edge structure (XANES) spectroscopy. *Soil Sci. Soc. Amer. J.* **59**, 1540-1548.
- Taylor G. J., Crowder A. A., and Rodden R. (1984) Formation and morphology of an iron plaque on the roots of *Typha latifolia* L. grown in solution culture. *Amer. J. Bot.* **71**, 666-675.
- USDA (1996) Soil Survey Laboratory Methods Manual, Report no. 42, Vol 3., Washington, D.C.
- Zachara J. M., Kittrick J. A., Dake L. S., and Harsh J. B. (1989a) Solubility and surface spectroscopy of zinc precipitates on calcite. *Geochim. Cosmochim. Acta* **53**, 9-19.
- Zachara J. M., Kittrick J. A., and Harsh J. B. (1989b) The mechanism of Zn^{2+} adsorption on calcite. *Geochim. Cosmochim. Acta* **52**, 2281-2291.
- Zachara J. M., Cowan C. E., and Resch C. T. (1991) Sorption of divalent metals on calcite. *Geochim. Cosmochim. Acta* **55**, 1549-1562.